Fiber-lattice accumulator design considerations for optical ΣΔ analog-to-digital converters

Phillip E. Pace, MEMBER SPIE
S. A. Bewley
John P. Powers, MEMBER SPIE
Naval Postgraduate School
Department of Electrical and Computer
    Engineering
1 University Circle
Code EC/PC
Monterey, California 93943
E-mail: pepace@nps.navy.mil

Abstract. Integrated optical sigma-delta (ΣΔ) analog-to-digital converters (ADCs) use a pulsed laser to oversample an input signal at two Mach-Zehnder interferometers. A fiber-lattice accumulator is embedded within a feedback loop around a single-bit quantizer to spectrally shape the quantization noise to fall outside the signal band of interest. Decimation filtering is applied to the quantizer output to construct the input signal with high resolution. Applications of integrated optical ΣΔ ADCs include digitizing wideband radio-frequency signals directly at an antenna (digital antenna). In this paper, a novel fiber-lattice accumulator design is presented, and a coherent simulation of an integrated optical first-order, single-bit ΣΔ ADC is reported. The accumulator leakage resulting from a mismatch in the optical circuit parameters is quantified. A time-domain analysis is presented, and the simulation results from an all-electronic ΣΔ ADC are presented for comparison. A frequency-domain analysis of a ten times oversampling ($n=4$ bits) simulation is used to compare the dynamic performance parameters, including the spurious-free dynamic range, signal-to-noise-plus-distortion ratio, and effective number of bits. The formation of image frequencies when the accumulator is overloaded (i.e., the optical amplifier gain is too large) is also investigated. © 2000 Society of Photo-Optical Instrumentation Engineers. [S0091-3286(00)03206-2]

1 Introduction

Sigma-delta (ΣΔ) modulators and their application in analog-to-digital conversion were first proposed in the 1960s but, due to their requirement for high oversampling rates, did not prove practical until recent improvements in technology. Today, the basic theory and operation of ΣΔ modulators is well documented in many research papers. Most investigations focus on the all-electronic implementation, with widespread applications developing in many areas of technology, including cellular phones and audio systems. A number of excellent ΣΔ tutorial papers have been published (e.g., Refs. 1–3), as well as several good books (e.g., Refs. 4–6). Although these architectures seem very straightforward, they are difficult to analyze rigorously, due to a quantizer in the feedback loop that generates a large nonlinearity. Consequently, the analysis of this nonlinear behavior has been of much interest, the first- through third-order architectures being the most studied.[7-9]

Few researchers have examined the concept of optical ΣΔ analog-to-digital converters (ADCs). A bulk-optic approach based on an oversampling and interpolative coding technique was described in Ref. 10. Using symmetric self-electro-optic effect devices (S-SEEDs) and error diffusion modulators, they propose an optical converter capable of sampling rates of up to 15 Gbit/s and providing resolutions of 8 and 16 bits at conversion rates of 983 and 117 MHz, respectively. Further investigation of the error diffusion modulator has been reported for both a first-order[11] and a

second-order system.[12] Due to the recent availability of wideband integrated optical (IO) components and high-pulse-repetition-frequency (PRF) mode-locked lasers, the oversampling of wideband signals has become increasingly feasible, giving the integrated optical approach a potential advantage over the contemporary all-electronic ΣΔ ADCs.[13] The IO approach uses pulsed lasers (currently PRFs of >100 GHz with time jitter <10 fs), interferometers, detectors, and comparators to oversample a signal and gives promise of extending the performance of the ΣΔ ADC into the very-high-frequency range and beyond. Decimation processing of the comparator outputs requires high-speed filtering, where high-temperature superconductor technology appears to be making a contribution with sampling speeds approaching the terahertz rate.[14] The driving force behind IO ΣΔ ADC technology is the large-bandwidth, high-resolution applications that are beyond the capability of the all-electronic ΣΔ architectures (limited typically to the audio range) and include digitizing wideband radio-frequency signals directly at an antenna (digital antenna).

Recently we reported an IO guided-wave ΣΔ converter design that used a pulsed laser to oversample an antenna signal at two Mach-Zehnder interferometers (MZIs).[15] In this device, a fiber-lattice accumulator is embedded within a feedback loop around a single-bit quantizer to spectrally shape the noise component so that the predominance of the noise falls outside the signal band of interest. Conse-

quently, it is expected that the time-and amplitude-jitter requirements of the oversampling laser can be relaxed compared to those required by the sampling source for an amplitude analyzing architecture. Decimation filtering is applied to the quantizer output to construct the antenna signal with high resolution. Due the integrated optical nature of the $\Sigma\Delta$ ADC approach, insensitivity to vibration and electromagnetic interference is also expected. Other advantages include separation of the sampling mechanism from the antenna signal and the elimination of the need to downconvert the signals before digitization. The simulation results reported in Ref. 15 compared favorably with the all-electronic architecture.

In our previous work, the fiber-lattice accumulator was modeled as an ideal device using an intensity simulation in order to evaluate the concept and detail the advantages of using MZIs within an IO $\Sigma\Delta$ converter. In this paper we extend these results by presenting a novel fiber lattice accumulator design and the results of a *coherent* IO $\Sigma\Delta$ simulation to more accurately evaluate the performance of a first-order single-bit architecture. The fiber-lattice accumulator design employs a two-state phase modulation to produce the proper interference between the input optical pulse and the recirculating optical pulse in order that they may be coherently combined. The phase modulation controls the optical accumulation, taking into account the sign of the sampled bipolar antenna signal appearing at the interferometer electrodes. For accumulation up, the resulting pulse amplitude is increased through constructive interference within the fiber-lattice directional coupler. For accumulation down, the pulse amplitude is decreased through destructive interference.

In this paper we also investigate the accumulator leakage resulting from a mismatch in the optical circuit parameters. A time-domain analysis is presented, and the simulation results from an all-electronic $\Sigma\Delta$ ADC are presented for comparison. A frequency-domain analysis of a ten times oversampling (n=4 bits) simulation is used to compare the ADC dynamic performance parameters, including the spurious-free dynamic range, signal-to-noise-plus-distortion ratio, and effective number of bits. The formation of image frequencies when the accumulator is overloaded (i.e., the optical-amplifier gain is too large) is also investigated.

The outline of the paper is as follows. Section 2 describes the all-electronic first-order single-bit $\Sigma\Delta$ ADC. The transfer function of the accumulator is presented, and the oversampling ratio is defined. Section 3 presents the signal-to-noise relationship for an oversampled system, along with the increase in bit resolution available. In Sec. 4 the IO first-order single-bit $\Sigma\Delta$ ADC architecture is presented, and Sec. 5 describes the coherent simulation and includes a detailed description of the fiber-lattice accumulator. In Sec. 6, the time-domain and frequency-domain simulation results for a $f = 0.2$-Hz signal are shown for an oversampling ratio of ten. The dynamic performance parameters for the two architectures are compared. In Sec. 7 we offer some concluding remarks and discuss some considerations necessary for hardware construction.
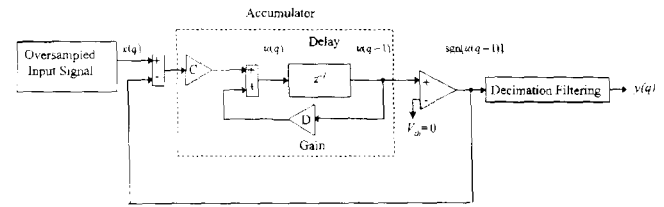
Fig. 1 Block diagram of an all-electronic first-order single-bit $\Sigma\Delta$ ADC.

2 All-Electronic $\Sigma\Delta$ ADC

Figure 1 shows the block diagram of a sampled-data, first-order, single-bit, all-electronic $\Sigma\Delta$ modulator.[2] These converters use a combination of oversampling, accumulation, and decimation filtering to demodulate the oversampled comparator output and construct the digital signal. The difference equation describing the first-order modulator is

$$u(q+1) = Du(q) + C\{x(q) - \text{sgn}[u(q)]\}, \tag{1}$$

where $x(q)$ is the oversampled input signal, C is a multiplying factor, D is the accumulator leakage coefficient, and

$$\text{sgn}[x] = \begin{cases} 1 & \text{for } x \geq 0, \\ 0 & \text{for } x < 0 \end{cases} \tag{2}$$

is the sign function. The transfer function for the accumulator (delay in the feedforward path) is

$$H = \frac{Cz^{-1}}{1 - Dz^{-1}}, \tag{3}$$

where z^{-1} is the delay operator. The dc gain of the accumulator is $H_0 = 1/(1-D)$. If the accumulator is ideal, then $D = 1$ (no leakage), $H_0 = \infty$, and the feedback connection forces the average value of the $\Sigma\Delta$ comparator output to equal the dc input. (Note that approximating the time-varying input signal by a dc signal is acceptable when averaged over a large time interval, due to the very high sampling rate of the converter.)

The signal is sampled at a rate defined by the *oversampling ratio* (OSR) given by

$$\text{OSR} = \frac{f_s}{2f_0} = \frac{\text{sampling frequency}}{\text{Nyquist frequency}}, \tag{4}$$

where f_0 is the signal bandwidth and f_s is the sampling frequency. The fast switching of the comparator modulates the signal and the noise. The noise component is spectrally shaped so that the predominance of the noise falls outside of the signal band of interest. The comparator output is processed by a decimation filter to (1) suppress the out-of-band high-frequency noise, (2) prevent aliasing of the out-of-band signal into the passband, and (3) downsample the filter's input signal (e.g., to Nyquist). This filtering usually involves a multistage decimation process (several filters and resampling stages), since the output of the modulator

Table 1 Oversampling relationships for $f_0 = 1$ Hz.

No. of octaves, E	Sampling freq. f_s (Hz)	Oversampling (OSR)
0	2	1
1	4	2
2	8	4
3	16	8

Fig. 2 Integrated optical first-order single-bit $\Sigma\Delta$ ADC.

represents the signal with the high-frequency modulation noise as well as its out-of-band components that dominate at the lower frequencies.

Due to the comparator (a nonlinear element) in the feedback loop, exact analysis of this simple structure is nontrivial, and many approaches to the analysis have been reported (see, e.g., Ref. 8). Also, the performance of the $\Sigma\Delta$ ADC tends to be insensitive to the presence of circuit imperfections,[4] lending itself nicely to an integrated optical approach.

3 Signal-to-Noise Relationships

3.1 Straight Oversampling

Oversampling a signal reduces the in-band quantization noise power n_0^2 falling into the signal band as

$$n_0^2 = \frac{2e_q^2 f_0}{f_s} = \frac{e_q^2}{\text{OSR}}, \tag{5}$$

where e_q^2 is the quantization noise power.[4] For each doubling of the sampling frequency, the in-band quantization noise power is reduced by 3 dB, providing an increase in resolution by 0.5 least-significant bit (LSB). The signal-to-noise ratio (SNR) for an oversampled system can be expressed as

$$\text{SNR} = 2^{n-1}\left(\frac{3f_s}{f_0}\right)^{1/2} \tag{6}$$

or

$$\text{SNR} = 6.02n + 1.76 + 10\log(\text{OSR}) \text{ dB}, \tag{7}$$

where n is the bit resolution of the ADC and f_0 is the signal bandwidth of interest. It is convenient to express the oversampling ratio as $\text{OSR} = 2^E$, where E is number of octaves (2×frequency) of oversampling.[3] Equation (7) is then

$$\text{SNR} = 6.02(n + 0.5E) + 1.76, \tag{8}$$

showing that we get 1/2 extra bit of resolution for each octave of oversampling. For example, with a three-octave oversampling system with $f_0 = 1$ Hz (OSR=8), we have $\text{SNR} = (n + 1.5)6.02 + 1.76$ and the SNR increases by 9 dB (or 1.5 bits), as expected. Table 1 shows the oversampling-octave relationship for the normalized $f_0 = 1$-Hz case. This table illustrates the sometimes confusing relationship between the OSR, the sampling frequency, and the number of octaves of oversampling.
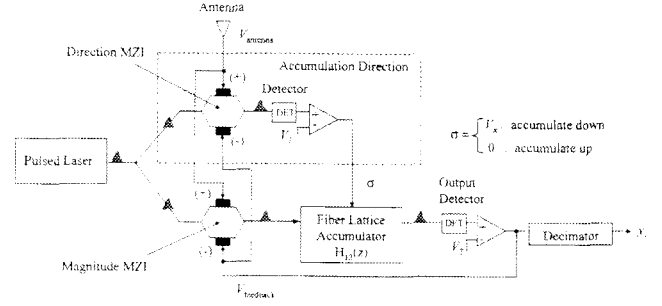
3.2 First-Order Architecture

The first-order oversampling architecture provides a more efficient means to enhance the SNR. The noise power for this architecture is

$$n_0^2 = \frac{e_q^2 \pi^2}{3(\text{OSR})^3}. \tag{9}$$

For each octave (doubling of the sampling frequency), the quantization noise power is decreased by 9 dB, giving 1.5 bits of extra resolution. The SNR for a first-order $\Sigma\Delta$ can be expressed as

$$\text{SNR} = 6.02n - 3.41 + 30\log(\text{OSR}) \text{ dB} \tag{10}$$

or

$$\text{SNR} = 6.02(n - 1.5E) \quad 3.41 \text{ dB}, \tag{11}$$

showing that we get 1.5 extra bits of resolution for every octave of oversampling. In general, the bit resolution of a first-order architecture can be approximated as[16]

$$n = 1.5\log_2(\text{OSR}) - \log_2\left(\frac{\pi}{\sqrt{3}}\right). \tag{12}$$

For example, an OSR of 10 results in a resolution of $n = 4$ bits.

4 Overview of Integrated Optical $\Sigma\Delta$ ADCs

The block diagram of a first-order, single-bit, integrated optical $\Sigma\Delta$ ADC architecture is shown in Fig. 2. The ADC is a coherent device that relies on oversampling an antenna signal (V_{antenna}) at two MZIs with a high-PRF laser. The accumulation of the sampled signal occurs prior to the output detector and quantizer using a fiber lattice $H_{12}(z)$. Since light intensity can only be positive, one MZI is used to sample and encode the antenna signal *magnitude* for accumulation in the lattice. The other MZI is used to sample the antenna signal polarity (the sampled signal's *direction* for accumulation). The MZIs are also used to subtract the output comparator's feedback signal (V_{feedback}) from the antenna signal V_{antenna}. The accumulation of the optical pulse from the magnitude MZI is accomplished via recirculation through the fiber lattice and coupling the polarity information σ from the direction MZI.[15] For $\sigma=0$, con-
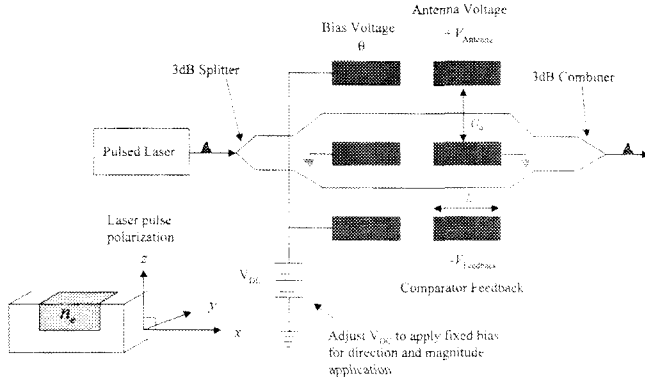
Fig. 3 Schematic diagram of a transverse LiNbO₃ MZI subtracting the antenna signal from the comparator feedback.

structive interference occurs within the accumulator (accumulate up). For $\sigma = V_\pi$, destructive interference occurs (accumulate down). The output pulse from the fiber lattice is detected and amplitude-analyzed with a high-speed comparator. The decimation filter is then applied to the comparator output (demodulation). Below, a coherent simulation of the device is described. The simulation gives an accurate representation of the integrated optical ADC performance.

5 Coherent ΣΔ Modeling

5.1 *Mach-Zehnder Interferometers*

The MZIs are used to efficiently couple the rf antenna signal into the optical domain and to subtract the feedback signal coming from the comparator ($V_{antenna} - V_{feedback}$). The optical input to the MZIs is the pulsed laser output. Figure 3 shows a schematic diagram of an MZI. The MZI consists of a 3-dB intensity splitter, two optical waveguides, electrodes, and an intensity combiner. The 3-dB intensity splitter separates the laser pulses into the two separate waveguides. The electrodes, which are positioned along the optical waveguide lengths, receive the antenna, feedback, and dc bias voltages and create electric fields in the optical waveguides. Each path of the MZI is affected separately, so that, when the pulses are recombined at the MZI output, an interference occurs. The voltages are applied separately to each path with opposite polarity (push-pull configuration), creating a voltage difference operation (for example, the antenna voltage is applied to one waveguide and the feedback voltage is applied to the other). The applied electric field changes the propagation coefficient of the laser pulse by changing the index of refraction of the optical waveguides as a function of the voltage. The two waveguides are then recombined at the output, resulting in an output laser pulse that is amplitude-modulated by the analog voltage (due to the constructive and destructive interference). If no voltage is applied to the electrodes, the pulses recombine coherently for a maximum output.

The transmissivity of an MZI (ratio of output intensity to input intensity) is a function of the phase difference $\Delta\phi$ between the waveguide paths[17]:

$$H_{MZI} = \frac{I_{out}}{I_{in}} = \frac{1}{2} + \frac{1}{2}\cos[\Delta\phi(v) + \theta], \tag{13}$$

where I_{out} and I_{in} are the output and input light intensities, respectively. The phase angle θ is a dc bias term that is used to adjust the quadrature point of the interferometer. A dc bias is applied separately to create both the magnitude and direction MZI transmissivity functions. As shown in Fig. 3, the pulsed laser light is assumed to be polarized along the crystallographic z axis, so the laser pulse sees the extraordinary index of refraction n_e and the strong electro-optic tensor coefficient r_{33}. Consequently the optical device is characterized as a transverse interferometer vice a longitudinal interferometer. For lithium niobate, $n_e^3 r_{33} = 3.28 \times 10^{-4}$ μm/V. This configuration allows a smaller voltage to affect the maximum phase change of π, making the device more efficient.[18] The expression often used for the voltage-dependent phase shift in a transverse lithium niobate push-pull interferometer is

$$\Delta\phi(v) = \frac{2\pi n_e^3 r_{33}\Gamma L_i v(t)}{G_a \lambda_L}, \tag{14}$$

where $v(t) = V_{antenna} - V_{feedback}$, Γ is the electro-optic overlap parameter, G_a is the interelectrode gap (m), L_i is the electrode length (m), and λ_L is the laser wavelength (m). In terms of V_π (the voltage required to shift the phase by π rad), the phase shift is

$$\Delta\phi(v) = \frac{\pi v(t)}{V_\pi}, \tag{15}$$

where

$$V_\pi = \frac{G_a \lambda_L}{2 L_i n_e^3 r_{33}\Gamma}. \tag{16}$$

The type of optical medium simulated in the MZI models was LiNbO₃. The optical parameters for LiNbO₃ and various other optical materials can be found in Ref. 17. LiNbO₃ MZIs are perfectly suited for the high-bandwidth applications (>40 GHz) associated with optical ΣΔ ADCs.

The transmissivity given in Eq. (13) is used to model the direction MZI. The magnitude MZI, however, requires a coherent intensity model, since the phase of the laser pulse must be preserved. This requires modeling the MZI waveguide paths separately (one as a phase modulator and the other left unaffected) to determine the modulation effects on the phase of each pulse as a function of the antenna voltage. The electric field in the path of the MZI containing the phase modulator is[18]

$$E_1 = \frac{A}{2}\cos[\omega_L t + \delta(v)], \tag{17}$$

where

$$\delta(v) = \frac{\pi v(t)}{V_\pi} \tag{18}$$
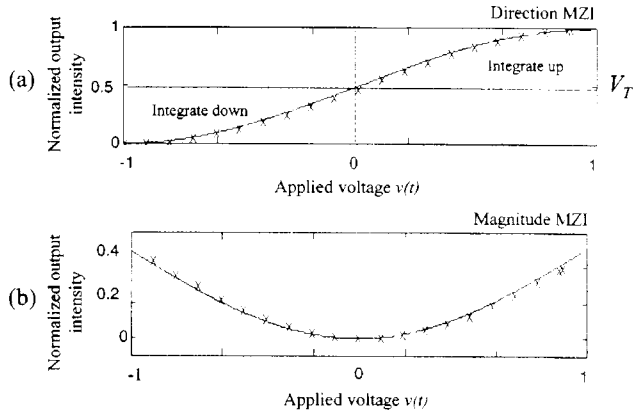
Fig. 4 Normalized MZI transmissivity as a function of the applied voltage for (a) the direction MZI and (b) the magnitude MZI. Shown are the phase-coherent simulated detections and Eq. (13) (solid line).

Fig. 5 Fiber-lattice accumulator design using a recoupling phase modulator.

is the phase modulation term, $v(t) = V_{\text{antenna}} - V_{\text{feedback}}$ is the total ac signal applied to the interferometer electrodes, and ω_L is the frequency of the laser. Rewriting Eq. (17) as

$$E_1 = \frac{A}{2}(\cos \omega_L t \cos \delta - \sin \omega_L t \sin \delta), \qquad (19)$$

we see that the phase modulation due to the antenna and feedback signal can be applied directly to the laser pulse. The MZI output is then
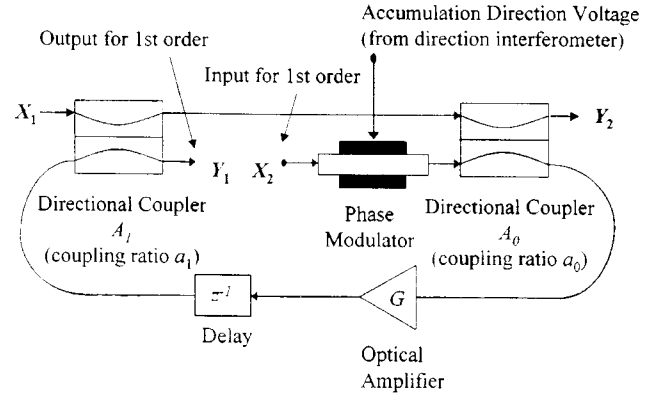
$$E_{\text{out}} = E_1 + E_2 = \frac{A}{2}(\cos \omega_L t \cos \delta - \sin \omega_L t \sin \delta)$$

$$+ \frac{A}{2}\cos \omega_L t, \qquad (20)$$

where E_2 is the electric field in the unmodulated waveguide path. Figure 4 shows the transmissivity (13) for both the direction and magnitude MZIs along with the detected pulse from the coherent model (20) for an applied ramp function from -1 to 1 V. Note that for $v(t) > 0$ V, the direction MZI detector output voltage (corresponding to the intensity I_{out}) exceeds the direction comparator's threshold voltage, $V_T = 0.5$. The direction comparator's output voltage ($\sigma = 0$ or V_π) is used to drive the phase modulator within the fiber lattice (accumulation up or accumulation down).

5.2 Fiber-Lattice Accumulator

The schematic diagram of the four-port fiber-lattice architecture is shown in Fig. 5.[19] The fiber-lattice structure consists of two directional couplers, an optical amplifier, a phase modulator, and a delay due to the length of the recirculating optical fiber. Blocks A_0 and A_1 are the directional couplers, with coupling coefficients a_0 and a_1. Also, X_1 and X_2 are the input ports, Y_1 and Y_2 are the output ports, G is the gain associated with the optical amplifier, and the z^{-1} block represents the optical delay of each pulse by one pulse repetition interval (1/PRF).

By choosing different combinations of directional coupler input and output ports in the fiber-lattice structure, one can select between a variety of known transmissivity functions.[20] Selecting input port X_2 and output port Y_1, while leaving X_1 and Y_2 unused, produces the power transmissivity

$$H_{12}(z) = \frac{(1-a_0)(1-a_1)Gz^{-1}}{1-a_0a_1Gz^{-1}}. \qquad (21)$$

where z^{-1} is the delay operator. Note that this is in the same form as the accumulator transfer function in the all-electronic device shown in Fig. 1,[4]

$$H(z) = \frac{Cz^{-1}}{1-Dz^{-1}}, \qquad (22)$$

where the multiplying factor $C = (1-a_0)(1-a_1)G$ and the leakage coefficient $D = a_0a_1G$.

For the correct operation of the fiber-lattice accumulator, the (power) coupling coefficients for the directional couplers (a_0, a_1) and the optical amplifier gain G must be matched ($D \approx 1$) to produce a monotonic linear response with a dc input. For example, a linear monotonic increase can be obtained with $a_0 = 0.4$, $a_1 = 0.6$, and $G = 4.166$ ($D = 0.9998$). A summary of matching values[21] for a_0, a_1, and G that give a linear response are listed in Table 2 and provide a good degree of hardware flexibility.

In any practical implementation however, optical circuit nonidealities will cause a mismatch in a_0, a_1, and G, resulting in a *leaky accumulator*. When the accumulator leakage is taken into account ($D \neq 1$), the input-versus-output plot is no longer linear. This is an important problem that has been actively studied. Feely and Chua[22] were able to quantify exactly the effects of accumulator leakage on the performance of the first-order $\Sigma\Delta$ modulator with a dc input. Park and Gray[23] analyzed a dynamical system representation of the leaky accumulator with a constant input. To investigate the effects of leakage from the fiber-lattice ac-

Table 2 Optical amplifier gain for various combinations of fiber lattice coupling coefficients a_0 and a_1 for linear monotonic response.[21]

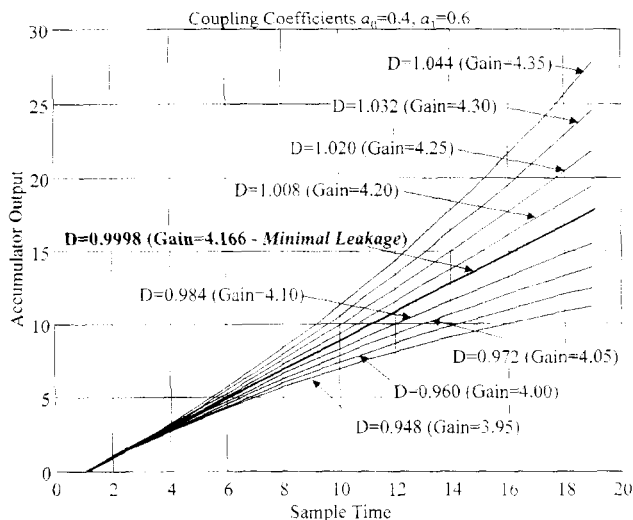|					Gain				
a_0	$a_1 = 0.1$	0.2	0.3	0.4	0.5	0.6	0.7	0.8	0.9
0.1	100	50	33.33	25	20	16.66	14.28	12.5	11.1
0.2	50	25	16.65	12.5	10	8.33	7.15	6.25	5.55
0.3	33.33	16.68	11.11	8.33	6.67	5.55	4.76	4.166	3.703
0.4	25	12.5	8.34	6.25	5	4.166	3.57	3.125	2.78
0.5	20	10	6.68	5	4	3.333	2.85	2.5	2.22
0.6	16.66	8.33	5.55	4.17	3.33	2.78	2.38	2.08	1.85
0.7	14.28	7.14	4.76	3.57	2.86	2.38	2.04	1.785	1.587
0.8	12.5	6.25	4.16	3.125	2.5	2.08	1.785	1.563	1.388
0.9	11.1	5.56	3.7	2.78	2.22	1.852	1.588	1.389	1.234

cumulator, Fig. 6 shows the fiber-lattice input versus output for a constant input of unity with various values of leakage coefficient D as a result of a nonoptimum optical amplifier gain ($a_0 = 0.4$, $a_1 = 0.6$). When the gain deviates from a matched value of 4.166, the input-output response becomes nonlinear. Figure 7 displays the fiber-lattice input versus output for various values of the leakage coefficient D as a result of a nonoptimum coupler coefficient a_0 ($G = 4.166$, $a_1 = 0.6$). The response due to a nonoptimum a_1 has a similar effect. Comparing Figs. 6 and 7, it is seen that the accumulator is most sensitive to variations in coupler coefficients.

We note that a change in the multiplying factor C (due to mismatch) does not affect the fiber-lattice accumulator's performance. Also, we note that besides the amplifier gain, the other primary parameter is the amplifier's *noise figure*. The noise figure is closely related to the spectral density of the forward-propagating amplified spontaneous emission (ASE) around the signal frequency as well as to the amplifier gain. As the signal propagates through the amplifier,

the signal-to-noise ratio deteriorates due to the addition of the spontaneous emissions of light from the erbium Er^{3+} ions (erbium-doped fiber amplifier).

To control the destructive and constructive interference, the coherent model of the fiber-lattice accumulator consists of a phase modulator positioned at the input of the fiber-lattice structure as shown in Fig. 5. The phase modulator within the fiber lattice recouples the direction and magnitude MZI outputs so the correct accumulation of the signal occurs. This is accomplished by phase-modulating the fiber-lattice input signal (magnitude MZI output) depending on the direction MZI comparator voltage σ (Fig. 2). That is, if the direction MZI detector voltage exceeds the direction comparator voltage threshold $V_T = 0.5$, the direction comparator output voltage is $\sigma = 0$ V (constructive interference). Otherwise the direction comparator output voltage to the fiber-lattice phase modulator is $\sigma = V_\pi$ and is the voltage required by the phase modulator to shift the magnitude MZI output pulse by π (destructive interference).

To calculate the output of the fiber-lattice phase modu-

Fig. 6 Fiber-lattice accumulator output for a dc input for various values of optical amplifier gain and corresponding leakage coefficient.
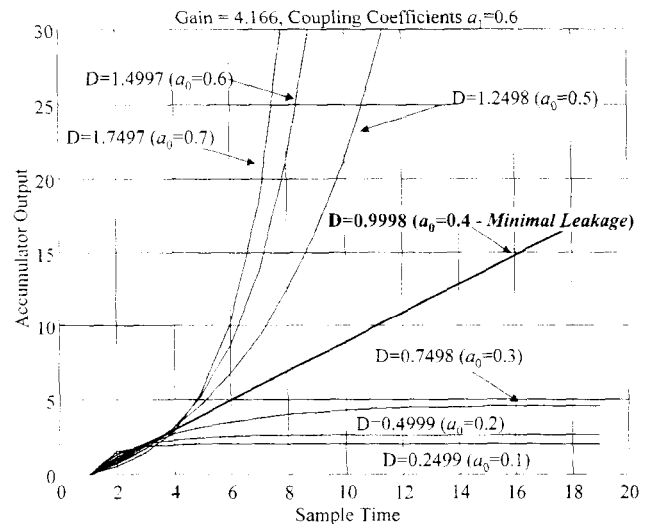
Fig. 7 Fiber-lattice accumulator output for a dc input with various values of mismatch in the coupler coefficient a_0 and corresponding leakage coefficient.

lator, the magnitude MZI output (20) is first rewritten as

$$E_{out} = E_1 + E_2 = \text{Re}\{\exp[j(\omega_L t + \delta)] + \exp(j\omega_L t)\}. \qquad (23)$$

The output of the fiber lattice phase modulator (E_ϕ) is then calculated by multiplying Eq. (23) by the direction comparator output:

$$E_\phi = \text{Re}\left\{ [\exp[j(\omega_L t + \delta)] + \exp(j\omega_L t)] \exp\left(j\frac{\pi}{V_\pi}\sigma \right) \right\}, \qquad (24)$$

where $\sigma = 0$ or V_π. The real part of Eq. (24) is the output of the fiber-lattice phase modulator and can be written as

$$E_\phi = \left[\cos \omega_L t \cos\left(\delta + \frac{\pi}{V_\pi}\sigma \right) - \sin \omega_L t \sin\left(\delta + \frac{\pi}{V_\pi}\sigma \right) \right]$$

$$+ \left[\cos \omega_L t \cos\frac{\pi}{V_\pi}\sigma - \sin \omega_L t \sin\frac{\pi}{V_\pi}\sigma \right]. \qquad (25)$$

If $\sigma = 0$, then no modulation of the magnitude MZI signal occurs, and both the input pulse and the recirculating pulse enter the directional coupler A_0 (Fig. 5) and combine coherently (addition). If $\sigma = V_\pi$, then the input signal from the magnitude MZI receives a phase shift of π and the two pulses add destructively (subtraction).

5.3 Output Photodetector

When the light exits the fiber-lattice structure, the electric field of the laser pulse must be detected and converted into a voltage. To model the photodetector, the first step is to square the output pulses as they exit the fiber lattice to determine their intensity. Next, each pulse is integrated individually. The signal's envelope is then calculated to determine the detector output voltage as

$$V(\Delta t) = I(\Delta t) = \int_{t_1}^{t_2} E_{\text{pulse}}^2(t)\, dt, \qquad (26)$$

where E_{pulse} is the electric field of the phase-modulated output pulse from the fiber lattice, $V(\Delta t)$ is the average detected voltage, $I(\Delta t)$ is the average pulse intensity, and Δt is the pulse length.

5.4 Output Comparator

The detected fiber-lattice output signal is amplitude-analyzed by the output comparator (Fig. 2). If the detected fiber-lattice output voltage is greater than 0.5 V, the comparator state $V_{\text{feedback}} = 1$ V; otherwise $V_{\text{feedback}} = -1$ V. The feedback voltage is then subtracted from the antenna signal, $v(t) = V_{\text{antenna}} - V_{\text{feedback}}$, at both the direction and magnitude MZIs.

5.5 Decimation Processing

Decimating the modulated output to obtain the high-resolution digital signal is accomplished in the same way as in the all-electronic $\Sigma\Delta$ architecture (it is lowpass-filtered and then resampled at the Nyquist rate). The only consideration prior to decimation is that the simulated laser pulse

repetition frequency (PRF) is significantly less than the computer sampling rate required to run the program efficiently. For example, if the simulated PRF of the laser is 5 Hz and the simulated light frequency within each pulse is 20 Hz, the minimum sampling rate required to generate each pulse is the Nyquist rate (40 Hz). Therefore, after modulation, the computer samples must be downsampled to equal the PRF of the laser prior to decimation; otherwise, the computer-calculated decimation function will assume the sampling rate to be the PRF and will not calculate the output correctly. Following downsampling, the normal decimation (lowpass filtering and resample) is calculated as in the all-electronic output.

6 Simulation Results

6.1 Time-Domain Analysis

Time-domain results are compared for the optical and the all-electronic $\Sigma\Delta$ ADC in Figs. 8 and 9. In Fig. 8 a ramp is applied as an input to both $\Sigma\Delta$ ADCs with $G = 4.166$, $a_0 = 0.4$, and $a_1 = 0.6$ ($D = 0.9998$—minimal accumulator leakage). The sampling frequency (PRF of the laser) was 4 Hz. (Only low PRFs are possible with the coherent model, due to computer simulation limitations.) Figure 8(a) shows the output of the decimation filtering state. Also shown for comparison is the input signal. Figure 8(b) shows the output of the accumulator (comparator input), and Fig. 8(c) shows the limit cycles from the output comparator (decimation filtering input).

In Fig. 9 a sinusoid with $f = 0.2$ Hz is applied (signal bandwidth $f_0 = 0.5$ Hz) as an input to both $\Sigma\Delta$ ADCs. The sampling frequency for this signal bandwidth was 10 Hz (OSR = 10, $n = 4$ bits). Figure 9(a) shows the output of the decimation filtering stage and the input signal for comparison. Figure 9(b) shows the output of the accumulator, and Fig. 9(c) shows the limit cycles from the output comparator. The initial step response at the beginning of the ramped output and the phase delay in the sinusoidal output are due to the initial charge-up of the lowpass filter during decimation. Note the amount of additional noise present in the optical ADC simulation results. This is due in part to the interaction time between the optical pulse and the signal being digitized.

Figure 10 shows a spectral comparison of the optical and the all-electronic $\Sigma\Delta$ magnitude spectrum for an OSR = 10. Both architectures resolved the input frequency and show the presence of a second harmonic. The optical ADC shows a higher noise level. The spurious-free dynamic range (SFDR) of the optical ADC is -30 dB. The SFDR of the all-electronic ADC is -44 dB. Using Eq. (10) with OSR = 10 and $n = 4$ gives a SNR of 51 dB for both architectures. To evaluate the signal-to-noise-plus-distortion (SINAD) ratio, the total harmonic distortion (THD) is first computed as

$$\text{THD} = 20 \log[(10^{2\text{ndHar}/20})^2 + (10^{3\text{rdHar}/20})^2 + \cdots]^{1/2} \text{ dB}. \qquad (27)$$

Since only the second harmonic is present, the THD in the optical ADC is -30 dB. The THD in the all-electronic ADC is -44 dB. The SINAD is defined as
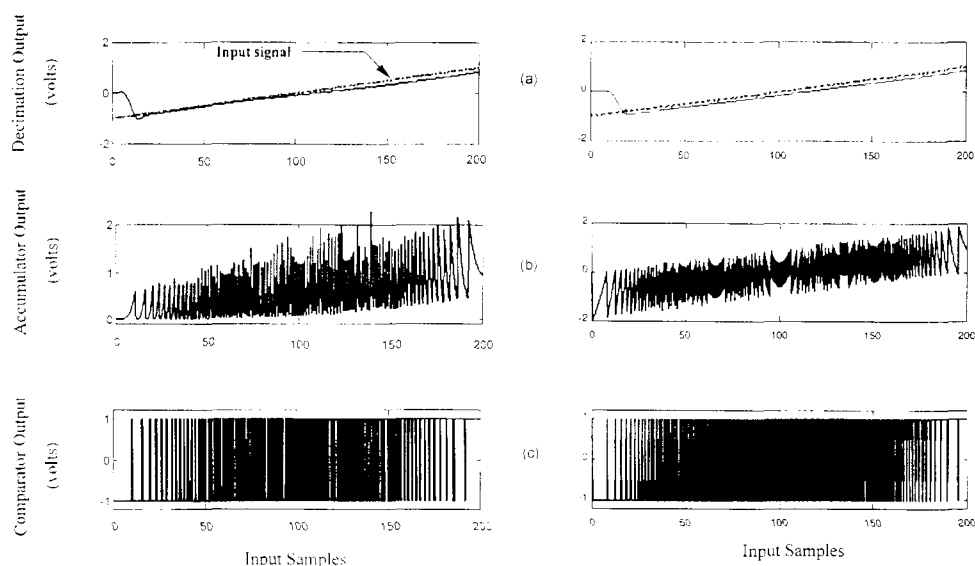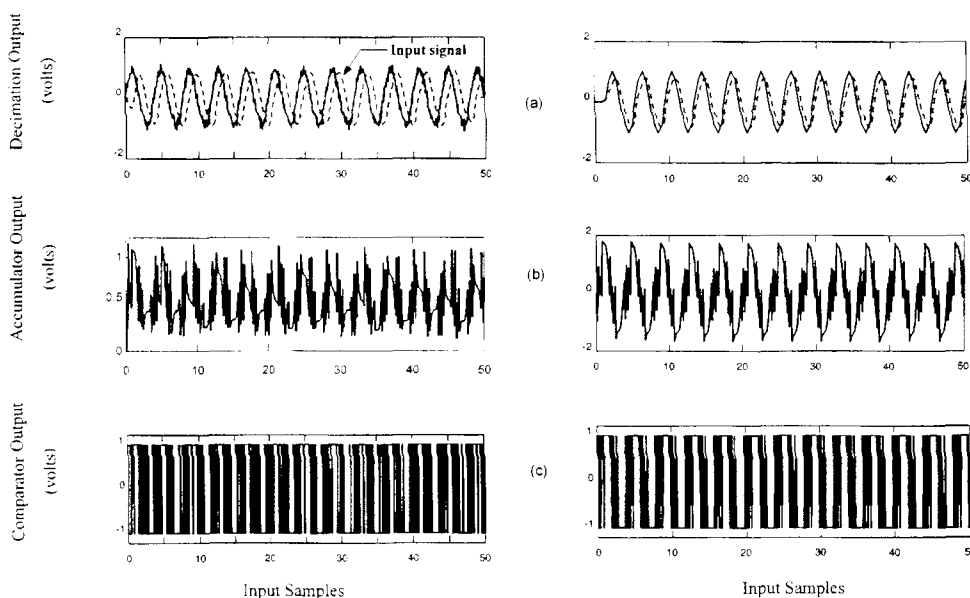
Fig. 8 Comparison of optical ADC and all-electronic ADC for an input ramp function. Each plot shows a corresponding stage in the $\Sigma\Delta$ architecture with (a) decimation output plotted with ADC input, (b) accumulator output stage, and (c) limit cycles from the output comparator.

$$SINAD = -20\log(10^{-SNR/10} + 10^{THD/10})^{1/2} \text{ dB}. \qquad (28)$$

For the optical ADC the SINAD is 29.9 dB and for the all-electronic ADC it is 43.2 dB. The effective number of bits (ENOB) can be calculated as

$$ENOB = \frac{SINAD + 3.41 - 30\log(OSR)}{6.02}, \qquad (29)$$

resulting in ENOB=0.55 for the optical ADC and ENOB =2.7 for the all-electronic ADC. The small number of effective bits in the optical ADC is due to the considerable amount of phase noise present in the simulation. This phase noise is a result of our low laser frequency (due to simulation constraints). Smaller pulse widths (smaller interaction time) and higher laser frequencies would improve these results. In Fig. 11, the gain of the optical amplifier was in-
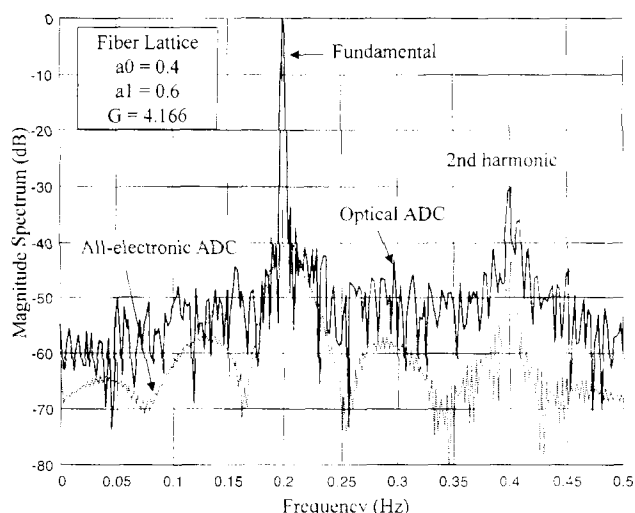

Fig. 9 Comparison of optical ADC and all-electronic ADC for an input sinusoid showing (a) decimation output plotted with ADC input sinusoid (dashes), (b) accumulator output stage, and (c) limit cycles from the output comparator.

Fig. 10 Comparison of optical ADC and all-electronic ADC with a 0.2-Hz input signal with OSR=10 (decimation in two stages, down-sampling by 5 and then 2).

creased from $G=4.166$ to $G=4.1663$. The additional gain resulted in an accumulator overload (pole too close to the unit circle), causing a phase imbalance within the accumulator. This phase imbalance generated image frequencies as shown in the figure. Note the continuing presence of the second harmonic.

7 Concluding Remarks

To correctly evaluate the performance of the fiber lattice within the optical $\Sigma\Delta$ design, a working reliable coherent computer model was described. All simulations were developed using Matlab and Simulink. The results confirm the correct operation of the integrated optical model in comparison with the all-electronic design. The phase-modulator–fiber-lattice-accumulator design demonstrated proper coupling of the magnitude and polarity signal information within the first-order $\Sigma\Delta$ device. Only low-frequency simulated signals were used to demonstrate the
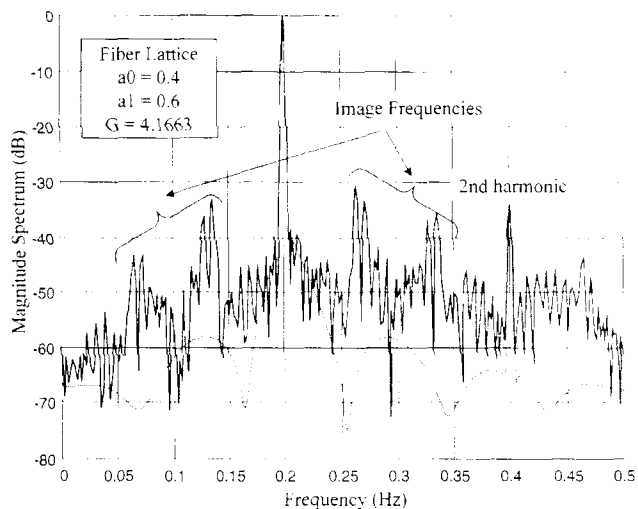
Fig. 11 Formation of image frequencies due to phase imbalance caused by optical-amplifier gain set to overload the accumulator.

optical $\Sigma\Delta$, due to computer limitations. However, the theory and concepts demonstrate the feasibility of the integrated optical $\Sigma\Delta$ ADC design for use in directly sampling higher bandwidths. Due to the high pulse rates associated with the pulsed laser, this could lead to direct digitization of microwave signals at significantly high oversampling ratios, resulting in increased signal resolution and improved sensor sensitivity. Second-order single-bit devices are also being investigated, as well as the effects of the optical amplifier's noise figure on the fiber lattice's performance.

Hardware construction of the fiber-lattice accumulator involves the use of an optical amplifier to supply the required gain. Also required is a piezoelectric fiber stretcher to fine-tune the feedback delay to maintain coherence within the lattice. Due to the small pulse widths being used, the use of a high-speed InGaAs optical detector is in order. A high-speed comparator (GaAs) can be used for the quantizer (the bandwidth of these devices is currently greater than 20 GHz). To decimate the output of the $\Sigma\Delta$ modulator section, high-speed high-temperature-superconductor unidirectional counters can be employed. Currently, two-junction SQUID D flip-flops are exceeding 1 THz and could provide an efficient method for filtering the gigahertz PRF of the mode-locked laser.[14]

References

1. B. E. Boser and B. A. Wolley, "The design of sigma-delta modulation analog-to-digital converters," *IEEE J. Solid-State Circuits* **23**, 1298–1308 (1988).
2. J. C. Candy and G. C. Temes, "Oversampling methods for A/D and D/A conversion," in *Oversampling Delta-Sigma Data Converters*, J. C. Candy and G. C. Temes, Eds., pp. 1–29, IEEE Press, New York (1992).
3. M. W. Hauser, "Principles of oversampling A/D conversion," *J. Audio Engin. Soc.* **39**, 3–26 (1991).
4. S. R. Norsworthy, R. Schreier, and G. C. Temes, *Delta-Sigma Data Converters—Theory, Design, and Simulation*. IEEE Press (1997).
5. S. Hein and A. Zakhor, *Sigma Delta Modulators, Nonlinear Decoding Algorithms and Stability Analysis*, Kluwer Academic Publishers, Boston (1993).
6. F. Wang and R. Harjani, *Design of Modulators for Oversampled Converters*, Kluwer Academic Publishers, Boston (1998).
7. S. H. Ardalan and J. J. Paulos, "An analysis of nonlinear behavior in delta-sigma modulators," *IEEE Trans. Circuits Syst.* **CAS-34**, 593–603 (1987).
8. R. Khoini-Poofard and D. A. Johns, "Analysis of $\Sigma\Delta$ modulators with zero mean stochastic inputs," *IEEE Trans. Circuits Syst., II: Analog Digital Signal Process.* **42**, 164–175 (1995).
9. L. A. Williams III and B. A. Wooley, "Third-order cascaded sigma-delta modulators," *IEEE Trans. Circuits Syst.* **38**, 489–497 (1991).
10. B. L. Shoop and J. W. Goodman, "Optical oversampled analog-to-digital conversion," *Appl. Opt.* **31**, 5654–5660 (1992).
11. B. L. Shoop and J. W. Goodman, "A first-order error diffusion modulator for optical oversampled A/D conversion," *Opt. Commun.* **97**, 167–172 (1993).
12. B. L. Shoop and J. W. Goodman, "Second-order cascaded optical error diffusion modulators for oversampled analog-to-digital converters," *Opt. Commun.* **102**, 125–132 (1993).
13. J. M. Butler, "Construction and measurement of an actively mode-locked sigma laser," Master's Thesis, Naval Postgraduate School, Monterey, CA (1998).
14. G. S. Lee and D. A. Petersen, "Superconductive A/D converters," *Proc. IEEE* **77**, 1264–1273 (1989).
15. P. E. Pace, S. J. Ying, J. P. Powers, and R. J. Pieper, "Integrated optical sigma-delta modulators," *Opt. Eng.* **35**(7), 1828–1836 (1996).
16. D. B. Ribner, "A comparison of modular networks for higher-order

oversampled $\Sigma\Delta$ analog to digital converters," *IEEE Trans. Circuits Syst.* **38**, 145–159 (1991).

17. R. C. Alferness, "Waveguide electro-optic modulators," *IEEE Trans. Microwave Theory Tech.* **MTT-30**(8), 1121–1137 (1982).
18. A. Yariv and Y. Yeh, *Optical Waves in Crystals,* John Wiley & Sons, New York (1984).
19. K. P. Jackson, S. A. Newton, B. Moslehi, M. Tur, C. C. Cutler, J. W. Goodman, and H. J. Shaw, "Optical fiber delay line signal processing," *IEEE Trans. Microwave Theory Tech.* **MTT-33**(3), (1985).
20. B. J. Moslehi, J. W. Goodman, M. Tur, and H. J. Shaw, "Fiber-optic lattice signal processing," *Proc. IEEE* **72**(7), 909–930 (1984).
21. P. E. Pace, A. F. Atherton, and J. P. Powers, "Integrated optical accumulators with applications in sigma-delta modulation," in *Proc. 7th Annual DARPA Symp. on Photonic Systems for Antenna Applications,* pp. 150–154, Naval Postgraduate School (1997).
22. O. Feely and L. O. Chua, "The effects of integrator leak in Σ-Δ modulation," *IEEE Trans. Circuits Syst.* **38**, 1293–1305 (1991).
23. S. J. Park and R. M. Gray, "Sigma delta modulation with leaky integration and constant input," *IEEE Trans. Inf. Theory* **38**, 119 (1992).
24. P. E. Pace, J. P. Powers, J. M. Butler, and S. Bewley, "NPS research in digital antennas," in *Proc. DARPA/ETO Photonic A/D Converter Technology Meeting,* MIT Lincoln Laboratory (1999).
25. P. E. Pace, S. A. Bewley, and J. P. Powers, "Fiber lattice accumulator design considerations for optical sigma delta digital antennas," in *Proc. 9th Annual DARPA Symp. on Photonic Systems for Antenna Applications,* Naval Postgraduate School (1999).

Phillip E. Pace is an associate professor in the Department of Electrical and Computer Engineering at the Naval Postgraduate School. He received the BS and MS degrees from the Ohio University in 1983 and 1986, respectively, and the PhD from the University of Cincinnati in 1990—all in electrical and computer engineering. Prior to joining NPS, he spent two years at General Dynamics Corporation, Air Defense Systems Division, as a design specialist in the Radar Systems Research Engineering Department. Before that, he was a member of the technical staff at Hughes Aircraft Company, Radar Systems Group, for five years. Dr. Pace has been a principal investigator on numerous research projects in the areas of high-speed signal processing and signal conversion architectures and currently directs the Naval Postgraduate School Center for Joint Services Electronic Warfare. He is a member of the Association of Old Crows and SPIE, and a senior member of IEEE.

S. A. Bewley graduated with a BS in chemistry from North Carolina State University in the spring of 1991. He was commissioned in the United States Navy from the North Carolina State University NROTC program at that time. Tours served include serving as the main propulsion assistant, USS Milwaukee (AOR 2), Norfolk, VA, 1991 to 1993, and as the combat information officer, USS Barry (DDG 52), Norfolk, VA, 1993 to 1996. Lt. Bewley earned the master's degree in applied physics with emphasis in electromagnetics and optics from the Naval Postgraduate School, Monterey, California. He is currently serving as operations officer on the USS John S McCain (DDG 56) stationed in Yokosuka, Japan.

John P. Powers is a professor of electrical engineering at the Naval Postgraduate School. He received his BSEE from Tufts University, his MSEE from Stanford University, and his PhD in electrical engineering from the University of California, Santa Barbara. He has been with the Department of Electrical and Computer Engineering at the Naval Postgraduate School since 1970. He also served as chairman of that department from 1987 to 1990, and was Dean of Faculty from 1994 to 1995 and Dean of Science and Engineering from 1995 to 1996. In 1974–1975 he was an exchange scientist at the University of Paris, working in the area of acoustic imaging. Professor Powers teaches in the areas of electro-optics, fiber optics, and electronics. He is the author of two editions of *Introduction to Fiber Optic Systems* and the editor of *Acoustical Imaging, Vol. 11.* Professor Power's research interests are in naval applications of fiber optics, acousto-optics, scalar-wave diffraction, and acoustic imaging.

A reprint from

OPTICAL
ENGINEERING